AFRL-RY-WP-TR-2020-0299

SEMI-CLASSICAL AND QUANTUM TRANSPORT FOR HIGH SPEED AND HIGH POWER ELECTRONIC AND OPTO-ELECTRONIC DEVICES

Matthew E. Grupen
Electronic Devices Branch (AFRL/RYDD)
Aerospace Components & Subsystems Division

OCTOBER 2020
Final Report

AIR FORCE RESEARCH LABORATORY
SENSORS DIRECTORATE
WRIGHT-PATTERSON AIR FORCE BASE, OH 45433-7320
AIR FORCE MATERIEL COMMAND
UNITED STATES AIR FORCE

REPORT DOCUMENTATION PAGE

Form Approved
OMB No. 0704-0188

1. REPORT DATE *(DD-MM-YY)*	2. REPORT TYPE	3. DATES COVERED *(From - To)*
October 2020	Final	1 January 2016 –1 September 2020

4. TITLE AND SUBTITLE
SEMI-CLASSICAL AND QUANTUM TRANSPORT FOR HIGH SPEED AND HIGH POWER ELECTRONIC AND OPTO-ELECTRONIC DEVICES

5a. CONTRACT NUMBER
17RYCOR495

5b. GRANT NUMBER

5c. PROGRAM ELEMENT NUMBER
N/A

6. AUTHOR(S)
Matthew E. Grupen

5d. PROJECT NUMBER
N/A

5e. TASK NUMBER
N/A

5f. WORK UNIT NUMBER
N/A

7. PERFORMING ORGANIZATION NAME(S) AND ADDRESS(ES)
Electronic Devices Branch (AFRL/RYDD)
Aerospace Components & Subsystems Division
Air Force Research Laboratory, Sensors Directorate
Wright-Patterson Air Force Base, OH 45433-7320
Air Force Materiel Command, United States Air Force

8. PERFORMING ORGANIZATION REPORT NUMBER

9. SPONSORING/MONITORING AGENCY NAME(S) AND ADDRESS(ES)
Air Force Research Laboratory, Sensors Directorate
Wright-Patterson Air Force Base, OH 45433-7320
Air Force Materiel Command

Air Force Office of Scientific Research Public Affairs (AFOSR)
875 North Randolph Street, Suite 325, Room 3112
Arlington, VA 22203

10. SPONSORING/MONITORING AGENCY ACRONYM(S)
AFRL/RYDD

11. SPONSORING/MONITORING AGENCY REPORT NUMBER(S)
AFRL-RY-WP-TR-2020-0299

12. DISTRIBUTION/AVAILABILITY STATEMENT
Approved for public release; distribution is unlimited.

13. SUPPLEMENTARY NOTES
PAO case number 88ABW-2020-3047, Clearance Date 6 October 2020. The U.S. Government is joint author of this work and has the right to use, modify, reproduce, release, perform, display, or disclose the work. Report contains color.

14. ABSTRACT

High speed power electronics and opto-electronics are central to a great number of Air Force and commercial applications. Software defined radio, cellular and satellite communications, missile transmitters, and defense-related radar are just a few examples of immediate technological requirements that make great demands on the power and frequency bandwidth of electronic components and circuits [1–6]. Other important applications such as optical communications, laser detection and ranging (ladar), laser imaging, diagnostics, material processing, and infrared countermeasures place stringent requirements on high power, high speed optical sources and detectors [7, 8]. Maintaining Air Force technological superiority requires exploiting applications like these to their fullest potentials.

15. SUBJECT TERMS
computer simulation

16. SECURITY CLASSIFICATION OF:			17. LIMITATION OF ABSTRACT:	18. NUMBER OF PAGES	19a. NAME OF RESPONSIBLE PERSON (Monitor)
a. REPORT	b. ABSTRACT	c. THIS PAGE			Matthew E. Grupen
Unclassified	Unclassified	Unclassified	SAR	25	19b. TELEPHONE NUMBER *(Include Area Code)* N/A

Final Laboratory Task Report 2016-2020

Title:	**Semi-classical and Quantum Transport for High Speed and High Power Electronic and Opto-electronic Devices**
Laboratory Task Manager:	Dr. Matt Grupen
Phone Number:	937-713-8191
Mailing Address:	AFRL/RYDD, 2241 Avionics Circle, Wright-Patterson AFB, OH 45433
E-Mail Address:	Matthew.Grupen@us.af.mil
AFOSR Program Manager:	Dr. Arje Nachman (AFOSR/RTB) Phone: 703-696-8427

1 Air Force Requirements & Research Objectives

High speed power electronics and opto-electronics are central to a great number of Air Force and commercial applications. Software defined radio, cellular and satellite communications, missile transmitters, and defense-related radar are just a few examples of immediate technological requirements that make great demands on the power and frequency bandwidth of electronic components and circuits [1–6]. Other important applications such as optical communications, laser detection and ranging (ladar), laser imaging, diagnostics, material processing, and infrared countermeasures place stringent requirements on high power, high speed optical sources and detectors [7, 8]. Maintaining Air Force technological superiority requires exploiting applications like these to their fullest potentials.

Meeting performance metrics demanded of advanced Air Force electronic and opto-electronic applications poses a challenging multiscale design problem. First, a material system must be selected to offer the appropriate electronic and/or optical properties. These may include good thermal conductivity as well as high critical electric field, electron mobility, and peak velocity [9], or large dipole moment matrix element combined with low Auger recombination [10]. If an appropriate material system with a suitable combination of properties can be identified, a device architecture based on this material must then be designed. It too must meet certain performance metrics, which might include high transconductance, output impedance, and breakdown voltage, or high quantum efficiency and optical responsivity [11]. The device must also be impedance matched with an output circuit or efficiently coupled to an external optical network. This design step can be further complicated by the highly nonlinear operating conditions, signal frequency dispersion, or unwanted harmonics. Concerns like these result in a costly and laborious design cycle that can benefit from predictive computational physics tools addressing one or more of the many design steps.

Because of the multiscale nature of the design process, its different aspects require very different computational tools. Material properties present a microscopic problem at the atomic level of a semiconductor's crystal structure that can be treated with various quantum mechanical approaches. Simulating the component level of the design process requires treating the dynamic interaction between electromagnetic (EM) fields and charges within the materials for realistic device structures on a macroscopic scale. Accuracy requires effective design tools include certain physical processes that reflect the conditions under which the components operate. For example, highly nonlinear operating conditions require a careful treatment of hot electron transport. Possible losses and memory effects require coupling hot electron transport to trapping and emission from crystal defects [12], and propagating wave effects at high frequencies require coupling it to full wave EM fields [13]. Capturing device-physics processes like these requires approaches different from those used for material properties. Integrating an electronic or opto-electronic component within a surrounding circuit/system represents yet another scale in the multiscale design problem with its own set of appropriate simulation approaches. Even the most numerically efficient physics-based device simulators still require too much computation to treat a large scale integration of active components. Instead, circuit simulations require compact device models, mathematical constructs using minimal numbers of fitting coefficients adjusted to match measured or simulated data.

The overarching objective of this research has been, and continues to be, developing methods for capturing the essential behavior at each design scale and communicating this information to the next level of the design process. The goal is quantitatively meaningful simulation of system behavior that may inform this design process and better achieve the performance metrics demanded by Air Force applications. AFOSR support has enabled considerable progress towards these ends. For example, it has resulted in an effective method

for incorporating microscopic material properties into a new hot electron transport model that combines accuracy and numerical efficiency not available in other academic or commercial simulators. In addition, it has produced a new EM field discretization scheme that allows the nonlinear hot electron transport to be fully coupled to Maxwell's propagating EM wave equations, resulting in the only electronic device simulation with full wave capabilities. Insights into how these physical effects impact circuit and system design have also been achieved. This report documents some of this progress. Section 2 details methods used for different parts of the multiscale problem, and Section 3 presents some of the notable results made possible by AFOSR support for this lab task.

2 Research Approaches

Length and time scales for different parts of the technology design process span many orders of magnitude ranging from atomic scales, for which quantum mechanical electron wave functions determine behavior, up through macroscopic device and integrated circuit scales, for which the behavior is virtually classical. As a result, different computational methods are required for different parts of the design process. For the microscopic level, there are various quantum mechanical approaches available to determine electronic and optical material properties. For example, the electronic band structure showing available electron energy states can be computed for better known electronic materials, e.g. Si and GaAs, using the empirical pseudopotential method (EPM) [14, 15]. Electron coupling to lattice vibrations can be computed from their relatively simple acoustic and optical phonon spectra [16] and from known deformation potentials [17] providing intravalley and intervalley electron-phonon scattering rates. Lesser understood materials, such as Ga_2O_3, may require ab initio methods such as density functional theory (DFT) [18, 19] available in public domain computational quantum chemistry software like Quantum Espresso (QE) and the Vienna Ab-initio Simulation Package (VASP). These codes can provide electronic band structures for complex crystal lattices like monoclinic β-Ga_2O_3. Additional features such as the Wannier electron phonon wave function [20] utility allow code suites like QE to compute electron-phonon coupling.

There are a variety of different approaches to physics-based active component level simulations. The non-equilibrium Green's function (NEGF) method [21] is a fully quantum mechanical treatment of charge transport which solves Schrodinger's equation for a Hamiltonian that includes electrostatics, band structure, and scattering potentials. It is fully correlated in space and time and spans the complete range of transport from diffusive to phase-coherent. However, it is prohibitively CPU intensive for 3D simulation of realistic device geometries. Full band ensemble Monte Carlo (EMC) is a semi-classical method that has been used for simulations of electronic devices [22–25]. It is a stochastic solution of the Boltzmann transport equation (BTE) that tracks large numbers of individual charged particles as they drift in real space under the influence of applied fields and scatter randomly in momentum space from various perturbing potentials. When EMC includes the material's full electronic band structure and all the relevant charge scattering mechanisms, it can produce accurate device simulations without relying on adjustable parameters. However, its stochastic algorithm is very computationally demanding and has difficulties resolving the highly disparate length and time scales of the different processes that can occur in electronic devices such as rapid phonon scattering combined with much slower defect ionization and lattice heating. Some more computationally efficient models are based on moments of the BTE. Moments of various orders produce different energy transport models, including hydrodynamics, and form the basis of highly successful commercial simulators [26–35]. These models can serve as effective design tools because they can reveal varying field strengths along with electron particle and energy densities within the device interior and draw connections between them and the device's terminal characteristics. However, important electronic material properties such as nonparabolic band structure and energy dependent phonon and impurity scattering are replaced with ad hoc adjustable parameters. This parameterized charge transport can compromise predictive accuracy and numerical stability [36–41]. Moreover, none of these transport models have been coupled self-consistently to full wave EM fields, which proves to be essential for high frequency electronics.

Working towards predictive computational capabilities, this lab task has developed new approaches to component-level simulation. This includes a hot electron transport model that can incorporate the quantum mechanical electronic material properties and a new discretization scheme that couples it to full wave EM fields. Devices are simulated by solving Ampere's (1), Faraday's (2), and Gauss's (3) laws, mobile electron continuity (4) and energy conservation (5), as well as the conservation of lattice energy (6),

$$\frac{\partial \epsilon \boldsymbol{E}}{\partial t} - q \sum_i \boldsymbol{J}_i = \nabla \times \boldsymbol{H} \tag{1}$$

$$-\frac{\partial \mu \boldsymbol{H}}{\partial t} = \nabla \times \boldsymbol{E} \tag{2}$$

$$\nabla \cdot \epsilon \boldsymbol{E} = q \quad N_D^+ - N_A^- - \sum_i n_i \Bigg) \tag{3}$$

$$-\frac{\partial n_i}{\partial t} = \nabla \cdot \boldsymbol{J}_i + C_i^n \tag{4}$$

$$-\frac{\partial E_i}{\partial t} = q\boldsymbol{E} \cdot \boldsymbol{J}_i + \nabla \cdot \boldsymbol{S}_i + C_i^E \tag{5}$$

$$-\rho C_p \frac{\partial T_L}{\partial t} = \nabla \cdot \kappa \nabla T_L - \sum_i C_i^E \tag{6}$$

where $\boldsymbol{E}$ and $\boldsymbol{H}$ are the electric and magnetic fields, N_D^+ and N_A^- are ionized impurity densities, n_i and E_i are the mobile electron particle and energy densities, respectively, $\boldsymbol{J}_i$ is the mobile electron particle flux, $\boldsymbol{S}_i$ is the total energy flux (i.e. kinetic energy flux plus electronic heat flow) for mobile electrons, C_i^n is the particle collision operator for electrons, C_i^E is the mobile electron energy collision operator, ρ is the mass density of the semiconductor crystal, C_p is its specific heat, κ is its thermal conductivity, and T_L is lattice temperature. Additional equations for mobile valence band holes can also be included to simulate bipolar devices such as p-n diodes or heterojunction bipolar transistors, but these will not be considered here. Steady state simulations neglect Ampere's and Faraday's laws and set all remaining time derivatives to zero. Quasi-static solutions are obtained by including the dynamic particle and energy densities and repeatedly solving (3)-(6) as the simulator steps through time. Full wave solutions solve the complete set of equations including Ampere's and Faraday's laws for rotational electric and magnetic fields.

Electron densities that can satisfy device equations (1)-(6) are computed using the Fermi kinetics transport model (FKT), which treats an electron ensemble as an ideal gas of particles with a piecewise Fermi-Dirac distribution,

$$f_i = \frac{1}{\exp\left(\frac{E-F_i}{k_B T_i}\right) + 1} \tag{7}$$

where k_B is the Boltzmann constant, F_i is an electron gas chemical potential/Fermi level, and T_i is its temperature [42]. Properties of an ideal gas depend on the electronic phase space it occupies. For example, the electron density is given by,

$$n_i = \int_{E_i} f_i(E) \left[\int_{\boldsymbol{k}_i} \frac{1}{4\pi^3} \frac{\delta(E_{\boldsymbol{k}} - E)}{|\nabla_{\boldsymbol{k}} E|} d\boldsymbol{k} \right] dE = \int_{E_i} f_i(E) \left[\int_{\boldsymbol{k}_i} \rho_{\boldsymbol{k}}(E) d\boldsymbol{k} \right] dE. \tag{8}$$

where $\boldsymbol{k}$ is the electron momentum vector, and the bracketed terms denote the density of electron states as determined by the gradient of electron energy in momentum space. Because an ideal gas is spherically symmetric is momentum space, its distribution function depends only on energy. As a result, the density of states can be integrated over all degenerate momentum vectors and saved as an energy spectrum for use in simulating carrier dynamics. Electron fluxes can be derived from odd moments of the BTE in the relaxation time approximation,

$$\frac{\partial f_i}{\partial t} = \frac{q}{\hbar} \boldsymbol{E} \cdot \nabla_{\boldsymbol{k}} f_i - \boldsymbol{v} \cdot \nabla f_i - \frac{f_i}{\tau_{\boldsymbol{k}}} \tag{9}$$

where $\boldsymbol{v}$ is the electron group velocity, and $\tau_{\boldsymbol{k}}$ is the momentum relaxation time [16]. The first moment gives the particle flux,

$$\boldsymbol{J}_i = \frac{1}{4\pi^3} \int_{\boldsymbol{k}_i} \boldsymbol{v} \tau_{\boldsymbol{k}} \left(q\boldsymbol{E} \frac{df_i}{dE} - \nabla f_i \right) \cdot \boldsymbol{v} d\boldsymbol{k} = \int_{E_i} \left[\int_{\boldsymbol{k}_i} \boldsymbol{v}\boldsymbol{v}^T \tau_{\boldsymbol{k}} \rho_{\boldsymbol{k}} d\boldsymbol{k} \right] \left(q\boldsymbol{E} \frac{df_i}{dE} - \nabla f_i \right) dE, \tag{10}$$

and the third moment gives the kinetic/internal energy flux,

$$\boldsymbol{K}_i = \frac{1}{4\pi^3} \int_{\boldsymbol{k}_i} E \boldsymbol{v} \tau_{\boldsymbol{k}} \left(q\boldsymbol{E} \frac{df_i}{dE} - \nabla f_i \right) \cdot \boldsymbol{v} d\boldsymbol{k} = \int_{E_i} E \left[\int_{\boldsymbol{k}_i} \boldsymbol{v}\boldsymbol{v}^T \tau_{\boldsymbol{k}} \rho_{\boldsymbol{k}} d\boldsymbol{k} \right] \left(q\boldsymbol{E} \frac{df_i}{dE} - \nabla f_i \right) dE. \tag{11}$$

Like electron density (8), electron fluxes (10) and (11) contain bracketed integrals over degenerate momentum vectors. These iso-energy integrals can also be precomputed and saved as energy spectra to simulate carrier dynamics.

The iso-energy integrals can be computed from a semiconductor's electronic band structure. Figure 1 shows how this can be done for GaN. Starting from the crystal's primitive lattice vectors, the reciprocal lattice can be computed. As indicated in Figure 1 (left), the reciprocal lattice for the GaN wurtzite crystal forms a set of simple tetrahedra, the circumcenters of which provide the crystal's first Brillouin zone. Also shown in Figure 1 (left) is a conformal mesh of tetrahedra filling the irreducible wedge. Crystal symmetry operations map this mesh throughout the rest of the Brillouin zone. Using EPM [15, 52], electron energy eigenvalues can be computed for momentum vectors identified by the Brillouin zone mesh points. Figure 1 (right) shows surfaces of constant electron energy for the first conduction band of GaN, labeled with the

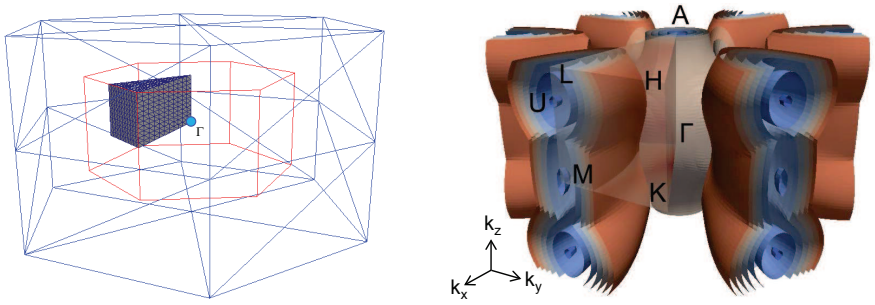

Figure 1: (left) A tetrahedral mesh (blue) is formed from the reciprocal lattice of the GaN wurtzite crystal. The circumcenters of the tetrahedra form a polyhedron (red) that defines the first Brillouin zone. Also shown within the Brillouin zone is another tetrahedral sub-mesh of the irreducible wedge. (right) Some electron energy iso-surfaces extracted from the electronic band structure computed on the Brillouin zone mesh points.

symmetry points at which local minima/valleys appear. Fermi gases of electrons are assigned to different valleys. Integrating energy gradients over the iso-energy surfaces provides the density of states spectrum required by (8) to determine the electron gas density in each valley. Combining these energy gradients with quantum mechanical electron scattering rates from Fermi's golden rule [16] provides the iso-energy integrals required by (10) to compute electron fluxes. Using the GaN electronic band structure and deformation potentials from Sarkar and Ghosal [53] produced flux iso-energy integrals shown in Figure 2. The figure also shows electron drift velocities versus electric field computed by FKT and compared with results computed with EMC [31, 54]. Electron drift velocities computed with Fermi kinetics compared favorably with results

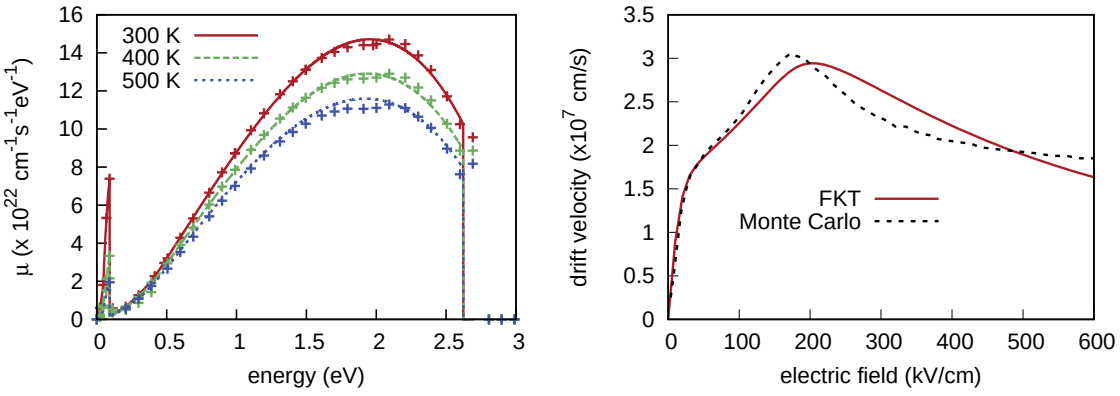

Figure 2: (left) The integral over degenerate momentum vectors from the bracketed term in (10) evaluated over Γ-valley electron energy iso-surfaces likes those shown in Figure 1 for different lattice temperatures. (right) Average velocity of the electrons assigned as Fermi gases to the GaN Brillouin zone valleys in Figure 1 versus applied electric field compared to ensemble Monte Carlo results from Benbakhti et al. [31] and Dessenne et al. [54].

from EMC, but FKT took a small fraction of the CPU time, making it well suited for simulating realistic high frequency device structures.

To enable simulation of larger scale integrated systems, the results of component simulations must be expressed in a more computationally efficient form with enough degrees of freedom to capture their complex behavior. This might be done empirically using table look-up to simply retrieve previously measured or simulated data [46]. The device characteristics could also be retrieved from a neural network trained

with the data [47]. Alternatively, the data might be reproduced with analytic functions whose shapes and adjustable parameters are sufficient to capture required features and trends [48]. All these approaches could be considered entirely empirical and described as behavioral models.

Other simplified device models suitable for circuit simulation appeal to the device's basic operating principles by defining an equivalent circuit that represents them through lumped parameter circuit elements. The result is known as a compact model, and details depend on the specific device being considered [49]. For example, a high electron mobility transistor (HEMT) is known to contain a high density of mobile electrons in a conducting channel that is modulated with a voltage applied to the gate contact. With this in mind, a compact model can define a channel charge in terms of a capacitor driven by a voltage related to the gate bias offset by a threshold parameter [50]. Assuming a linear voltage drop along the channel defines an electric field which can be combined with the channel electron density and an electron mobility parameter to compute a channel current. This simple representation can exhibit transistor behavior. Adding additional adjustable parameters to represent other features such drain access resistance, parasitic capacitances, and temperature dependencies can enable the model to reproduce measured device characteristics in a computationally efficient manner. Although key model parameters must be extracted from experimental measurements, they are used to express the device's underlying operating principles. In this sense, such compact device models could be considered not entirely empirical and may indicate how some design changes could affect performance. As a result, this lab task investigates these compact models for circuit simulation purposes.

3 Program Accomplishments

Based on computational physics approaches described above, this lab task continued its progress on different levels of the multiscale design process. This section details some of the achievements for different aspects of the problem, including the microscopic material properties, component-level simulation, as well as circuit design.

3.1 Electronic Material Properties

To realize effective computational tools for electronic and opto-electronic application development, it is necessary they can accommodate a variety of technologically important material systems. Some successes had previously been reported for GaAs and GaN technologies. Continued research has worked to broaden the range of material systems.

Gallium oxide Ga_2O_3 has gained attention for power electronics and other applications because of its wide band gap, second only to diamond among semiconductors. It occurs in five different polymorphs with different structural, electronic, and optical properties, but β-Ga_2O_3 is the most stable. It forms a monoclinic crystal lattice, which is a distorted cubic structure that provides the closest packing. Its modest mobility and poor thermal conductivity are partially offset by its very high critical breakdown field. For a given design voltage, this allows a thinner device and possibly improved efficiency. As a result, β-Ga_2O_3 is considered for applications such as display technologies, photovoltaics, chemical sensors [55, 56], and high voltage electronics, e.g. switching memories and heavy-duty electric motors [57, 58]. To undertake simulating a device made from β-Ga_2O_3, electron energy isosurface integrals for the FKT model must be computed. This requires using the crystal's primitive lattice vectors to compute the reciprocal lattice vectors and then using the reciprocal vectors to compute the first Brillouin zone. Although this procedure was also required for previously considered materials, the β-Ga_2O_3 distorted monoclinic lattice required a generalized algorithm based on the geometry of intersecting perpendicular bisector planes. The resulting Brillouin zone was then filled with conformal tetrahedra like those shown in Figure 3 (left).

To compute electronic band structure at mesh points of the β-Ga_2O_3 Brillouin zone, the Vienna Ab initio Simulation Package (VASP) was investigated. VASP produces solutions to the many-body Schrodinger equation using density functional theory (DFT) with different possible choices of potentials and functionals. Figure 3 (middle) shows electron eigenenergies for different points in the Brillouin zone using the Tran-Blaha modified Becke-Johnson exchange-correlation potential and using the Heyd-Scuseria-Ernzerhof hybrid functional. Phonon dispersions, like those shown in Figure 3 (right), are required to compute electron scattering processes. They can be computed with perturbation DFT available in the QE computational chemistry suite installed on AFRL HPC platforms. The phonon dispersions can then be imported into QE's electron-phonon Wannier utility to compute the electron-phonon interaction throughout the Brillouin zone. These results provide the information needed for solving a stationary Boltzmann equation and for computing the isosurface integrals.

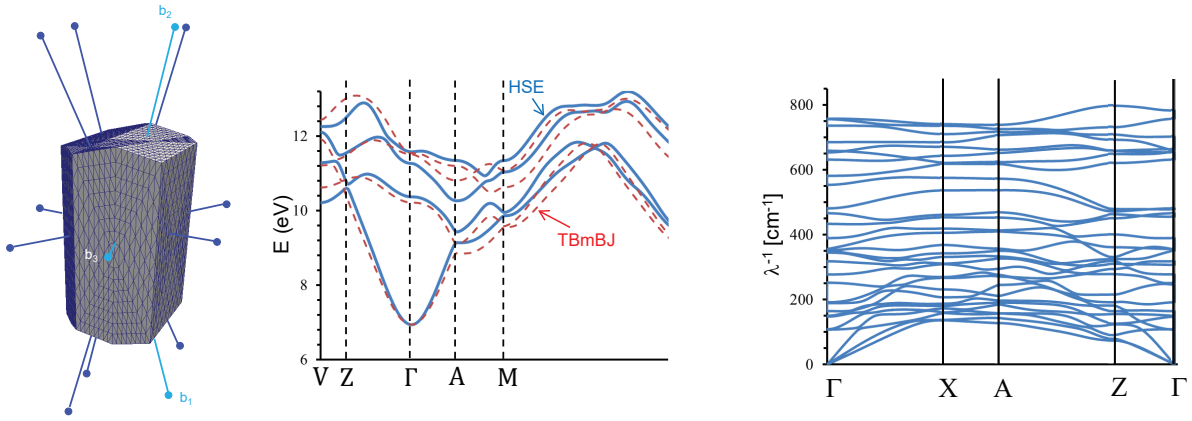

Figure 3: (left) Conformal tetrahedral mesh for first Brillouin zone of monoclinic β-Ga_2O_3 to use for computing the electron energy isosurface integrals required for full band Fermi kinetics simulation of devices made with this material. (middle) Electronic band structure for monoclinic β-Ga_2O_3 computed with VASP. 'TBmBJ' uses the Tran-Blaha modified Becke-Johnson exchange-correlation potential, and 'HSE' uses the Heyd-Scuseria-Ernzerhof hybrid functional. (right) The phonon dispersion for β-Ga_2O_3 computed with the Quantum Espresso computational chemistry suite.

Because of the β-Ga_2O_3 crystal's large and complex primitive unit cell, accurate computation of some electronic properties can require DFT with hybrid exchange correlation energy functionals involving expensive Hartree-Fock calculations of nonlocal exchange energies [19, 59]. When investigating higher dimensional defects (dislocation or interface), interaction between defects, or configuration order in alloys, a more computationally efficient approach addressing larger scale systems may be necessary. Semi-empirical methods with various approximations of electronic integrals can lead to significant reduction in computational demand. The density functional tight binding (DFTB) method is one popular choice derived from DFT [60]. A new parameter set was constructed and optimized for the bulk electronic properties and lattice structure of β-Ga_2O_3. It was also tested for other properties such as surface energy and point defect formation energy.

The first step of parameterization was the pseudoatomic orbital (PAO) of gallium and oxygen. Assuming a quadratic confinement potential of $V_{\text{conf}}(r) = (r/r_0)^2$, the confinement length r_0 becomes an independent parameter of PAO optimization. For a specified confinement length, a set of PAOs (s and p orbitals of oxygen along with s, p, and d orbitals of gallium) can be computed. Using those PAO, Slater-Koster (SK) functions were calculated as functions of separation distance between PAOs [61], resulting in electronic band structure agreeing reasonably with more computationally expensive DFT results obtained with the hybrid functional HSE06 and allowing investigation of higher dimensional oxygen defects. Figure 4 shows the formation energy of oxygen vacancy defects. All three types of vacancies assume neutral states stable when the Fermi level is near the conduction band. The donor states of +2 valence become stable in the midgap. The transition level, $\epsilon(+2/0)$, is deeper than 1 eV from the conduction band for all three types of oxygen sites. Such observations are in accordance with other DFT studies [59, 62]. However, the formation energies of oxygen vacancies are generally overestimated compared to the reported values of some previous studies. Figure 4 also shows the formation energies of gallium vacancy defects, which are in good agreement with the literature [59].

Additional ab initio computational research has investigated electron-phonon coupling in β-Ga_2O_3, which is essential for simulating device structures incorporating this material [63]. Here, QE was used for ground state DFT as well as the corresponding perturbation DFT for dynamical lattice properties. After computing electron and phonon dispersions, the electron-phonon Wannier (EPW) software package, including a recent extension for polar materials [64], was used to compute the electron-phonon coupling matrix elements for different degenerately doped oxide materials. The resulting electron-phonon scattering rates are shown in Figure 5. The strong temperature dependence illustrates the rapid occupation of higher energy phonon modes. Integrating these scattering rates over electron band structure energy isosurfaces may enable macroscopic simulation of β-Ga_2O_3 device structures.

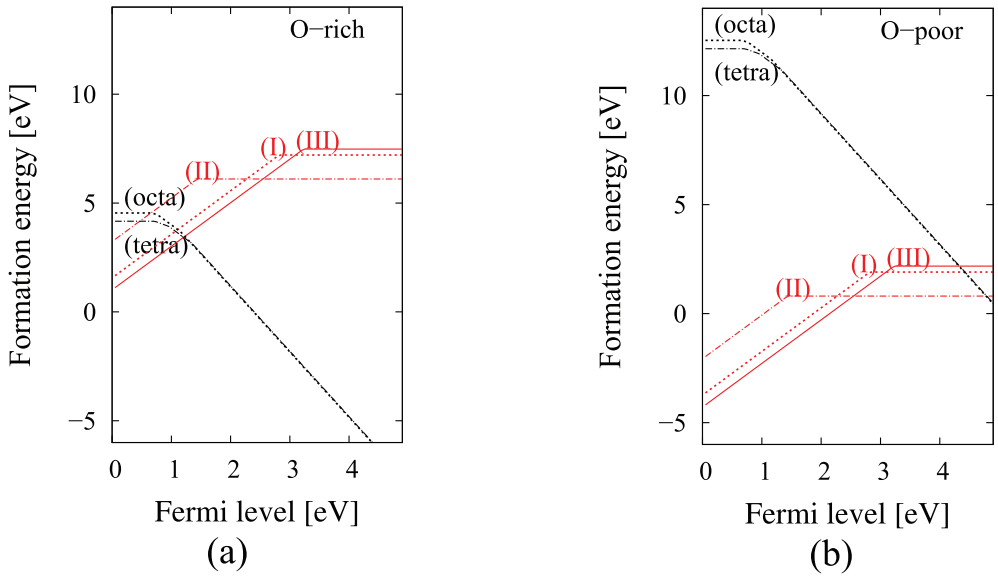

Figure 4: Formation energies of point defects in β-Ga_2O_3 plotted against the Fermi level for (a) oxygen rich and (b) oxygen poor conditions. Red lines are for oxygen defects. Black lines are for gallium vacancies. (tetra) is for vacancy at the Ga(I) site, and (octa) is for vacancy at the Ga(II) site of the monoclinic unit cell.

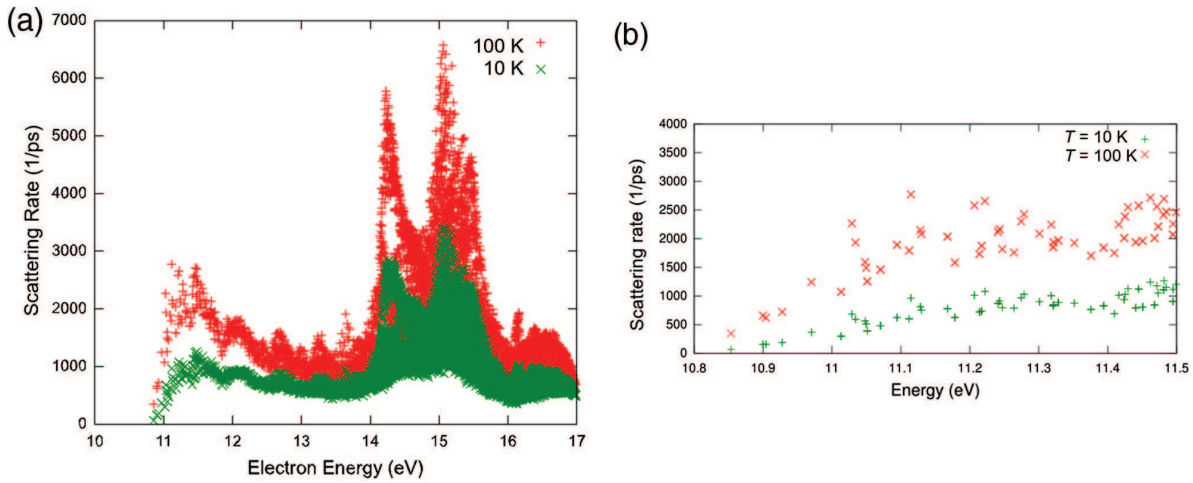

Figure 5: Electron-phonon scattering rates in the full range of β-Ga_2O_3 conduction bands (a) and in a small window near the conduction band minimum (b) for $T = 10$ and 100 K.

3.2 Component-Level Simulations

In addition to considering additional material systems, this lab task also continued its work on macroscopic device-level simulation. This included an investigation of the numerical properties of the FKT hot electron model. To get some sense of the convergence characteristics of the nonlinear FKT equations, convergence was quantified by defining an L^2 error,

$$\epsilon_{ik} = \sqrt{\frac{\sum_j w_j [\tilde{u}_{ij,k} - u_{ij,k}]^2}{\sum_j w_j u_{ij,k}^2}}, \tag{12}$$

and evaluating it on a series of meshes with varying density. Here, $\tilde{u}_{ij,k}$ is the i^{th} solution variable defined on the j^{th} element of the k^{th} mesh after it has been interpolated onto the most dense mesh, whose solution variables are $u_{ij,k}$. The weighting factor w_j is the Voronoi volume associated with node j. An approximate

order of convergence p_k was then determined by,

$$\epsilon_k = \sqrt{\sum_i \epsilon_{ij}^2} < C N_k^{-p_k}, \tag{13}$$

where N_k is the number of independent variables and C is a constant that best fits the global errors. The data shown in Figure 6 (left), computed for a generic transistor under saturation conditions, suggests approximately first order convergence for the FKT method as it is currently implemented.

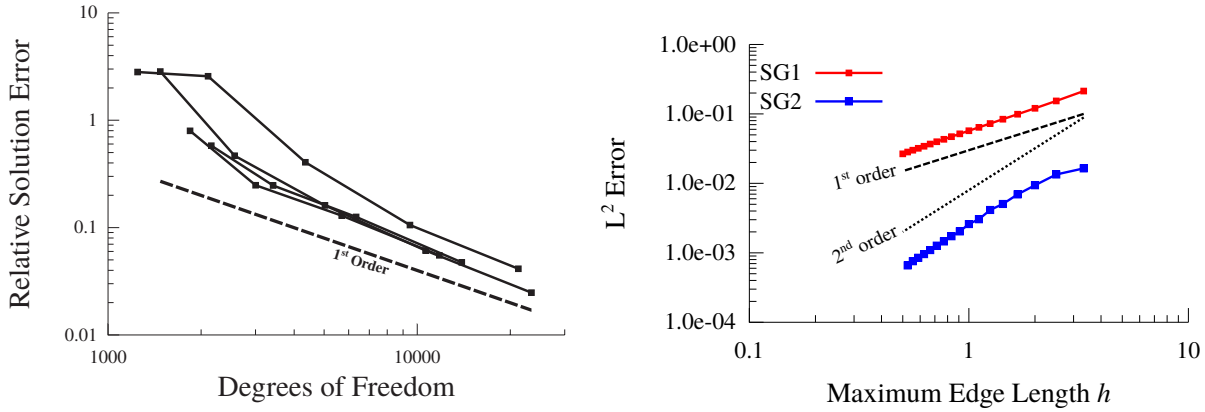

Figure 6: (left) Integrated errors, calculated with (13) for a MESFET biased in saturation and simulated with different mesh densities. (right) Order analysis of the FKT particle flux reconstruction. Errors labeled SG1 corresponded to discretized fluxes computed from (15) and those labeled SG2 correspond to (16). As expected, the SG1 particle fluxes exhibit first order convergence, and the SG2 particle fluxes exhibit second order convergence.

To explore possible improvements in convergence, higher order discretization was considered, principally the FKT particle and energy fluxes. Simulations to date have used the Scharfetter-Gummel flux discretization scheme [51]. It is a highly effective method based upon the assumption that a flux density of the form,

$$J(r) = a_1 n(r) + a_2 \frac{dn(r)}{dr}, \tag{14}$$

is constant along the length L of any mesh edge in the simulation domain, where $0 < r < L$. The constant flux assumption allows (14) to be solved in terms of the electron densities at the edge's two nodes, n_0 and n_1,

$$J = -\frac{a_2}{L}[B(x)n_0 - B(-x)n_1]; \qquad B(x) = \frac{x}{e^x - 1}, \tag{15}$$

where $x = a_1 L/a_2$. The resulting flux is numerically robust and consistent with the constant electric field projections assumed on mesh edges. However, these piecewise constant assumptions result in the 1st order convergence suggested by Figure 6.

To test higher order discretization, the flux was assumed piecewise quadratic,

$$J_2(r - r_0)^2 + J_1(r - r_0) + J_0 = a_1 n(r) + a_2 \frac{dn(r)}{dr}, \tag{16}$$

and solved using the electron densities as well as their gradients. The resulting discretized flux is given by,

$$J = -\frac{a_2}{L}\left[B_1(x)n_0 - B_2(x)n_1 + LB_3(x)\frac{dn_0}{dx} - LB_4(x)\frac{dn_1}{dx}\right] \tag{17}$$

$$B_1(x) = \frac{x\left[4 + 3x + e^x(x-4)\right]}{4\left[2 + e^x(x-2) + x\right]}$$

$$B_2(x) = \frac{x\left[4 + x + e^x(3x-4)\right]}{4\left[2 + e^x(x-2) + x\right]}$$

$$B_3(x) = -\frac{4 + x(x+3) + e^x(x-4)}{4\left[2 + e^x(x-2) + x\right]}$$
$$B_4(x) = -\frac{4 + x - e^x[4 + x(x-3)]}{4\left[2 + e^x(x-2) + x\right]}.$$

An easy way to see the effects of this higher order discretization is to assume some spatial variation in the electric fields as well as the carrier particle and energy densities so that (14) can be evaluated analytically and compared to the approximations provided by (15) and (16) for different mesh sizes. An example of this comparison in Figure 6 (right) shows that the higher order discretization can, in principle, produce a better approximation. However, the higher order discretization scheme must be implemented within a realistic device simulation to test if its encouraging numerical behavior persists over a full range of highly nonlinear operating conditions.

In addition to considering possible numerical improvements, further research also applied the simulation to real-world applications such as various RF switches. Wide band RF subsystems with minimal power dissipation and small form factors are needed to counter emerging Air Force threats, and ongoing progress in solid-state electronics may be a path towards these goals. GaN HEMTs can address the RF amplification needs of DoD systems, but trade offs between performance and miniaturization persist. For example, when configured for amplification, the HEMT can provide power gain across a wide bandwidth, but as switches they can introduce RF loss that limits subsystem power and operating frequency. Furthermore, transistor-level characteristics such as threshold and driving voltage are largely fixed by the epitaxial structure, impeding realization of on-chip low-power (E/D) logic and analog circuits.

Functionality not available on a monolithic microwave integrated circuit (MMIC) can be incorporated off-chip, although usually with increased size, complexity, and cost. Expanding the library of circuit elements available in the MMIC would provide increased design flexibility, thereby enabling new circuit functionality and improved microsystem performance within a small and manufacturable form factor. To attain higher levels of integration for RF microsystems, the DVSI/FKT simulation tools may be used to help assess the trade space between monolithic and off-chip RF control devices. Figure 7 (left) shows a potential RF switch design whose switching capabilities are determined by voltage control of a 2DEG density maintained at a

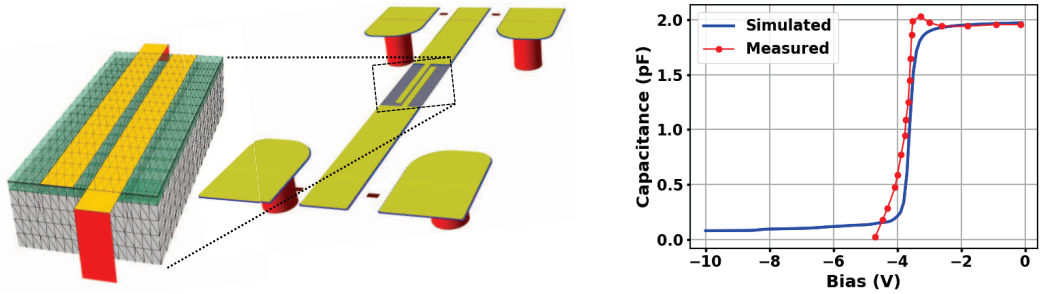

Figure 7: (left) A gateless HEMT structure containing a GaN/AlGaN interface which induces a 2DEG whose density can be controlled with dc bias conditions. (right) Voltage control of the 2DEG significantly affects the device's capacitance, thereby allowing it to act as a voltage-controlled capacitive switch.

GaN/AlGaN interface below the device surface. Since this varactor's electromagnetic behavior is controlled by manipulating mobile charges within the device, the tools developed by this lab task are well suited for its simulation. Figure 7 (right) shows good agreement between simulated and measured capacitance versus applied bias voltage. Further simulations can investigate the effects of design changes to improve the device's RF switching performance.

Along with investigating device design variations, other simulations were used to investigate certain aspects of semiconductor device physics that are not entirely understood. Full wave electromagnetics discretized with DVSI and combined with FKT charge dynamics has demonstrated accurate simulations up through the mm-wave frequency range [43]. However, considering still higher frequencies requires a more careful look at the limits of diffusive transport. As described in Section 2, mobile electron fluxes used in FKT can be obtained from the first moment of the Boltzmann equation,

$$\boldsymbol{J} + \bar{\tau}\frac{\partial \boldsymbol{J}}{\partial t} = \frac{1}{4\pi^3}\int_{\boldsymbol{k}} \boldsymbol{v}\tau_{\boldsymbol{k}}\left(q\boldsymbol{E}\frac{df}{dE} - \nabla f\right)\cdot \boldsymbol{v}d\boldsymbol{k}, \tag{18}$$

but unlike (9), this moment of the BTE includes $\bar{\tau}$, which is a weighted average of the momentum relaxation lifetime $\tau_{\boldsymbol{k}}$ computed from mobile electron scattering rates. For high speed semiconductor devices, $\bar{\tau}$ can be subpicosecond and $\bar{\tau}\partial \boldsymbol{J}/\partial t \approx 0$ up through mm-wave frequencies. At higher frequencies, this term is non-negligible and can significantly affect device behavior.

A version of FKT was developed to incorporate the limits momentum relaxation places on diffusive transport. A discretization scheme was developed for fluxes of the form given by (18), and it was first tested with simple lossy transmission lines. Figure 8 shows results for different values of $\bar{\tau}$. The simulated

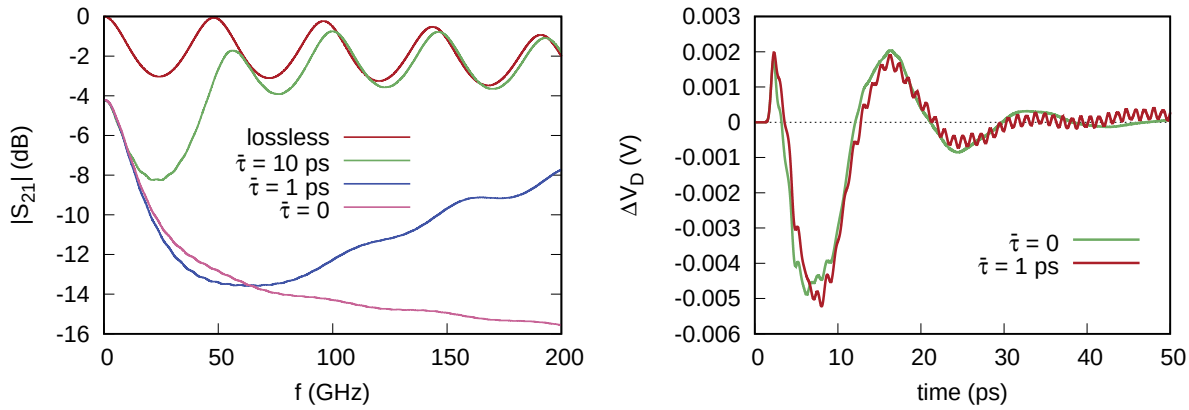

Figure 8: (left) The magnitudes of S-parameter S_{21} for a rectangular transmission line simulated as lossless, ideally lossy $\bar{\tau} = 0$, and lossy with finite electron momentum relaxation time. (right) Time dependent voltage at drain of GaN HEMT with gate length $L_G = 0.1$ μm and a $\sigma = 0.1$ ps Gaussian input voltage on the gate simulated with different average momentum relaxation lifetimes. The red curve exhibits rapid THz oscillations that persist long after the energy injected by the Gaussian signal has dissipated.

S-parameters S_{21} in Figure 8 (left) show how $\bar{\tau}$ places frequency limits on diffusive transport. When there are no mobile charges in the substrate, the transmission line is ideally lossless and produces the $|S_{21}|$ shown in red. When the substrate is conductive but $\bar{\tau} = 0$, it can be considered ideally lossy in that mobile charge momentum randomizes instantly. The corresponding S-parameters in Figure 8 show significant current shunted through the lossy substrate and away from the transmission line output. The figure also shows S-parameter for lossy substrates and $\bar{\tau} > 0$, revealing how the limits of diffusive transport cause the device to act ideally lossy at low frequencies and then approach ideally lossless behavior at sufficiently high frequencies. This would represent a fundamental change in an active electron device from nonlinear amplification of electrical signals to passive storage of EM energy.

The momentum relaxation limits to diffusive transport were also included in the FKT simulation of a short gate length ($L_G = 0.1$ μm) transistor. For such a short length, $\bar{\tau}$ can be small enough to allow rapid mobile charge fluctuations but still larger than the charge transit time through the channel beneath the gate. This near ballistic transport has been observed to produce spontaneous oscillations in the drain current [44,45]. To test this, static simulations of the short channel transistor were performed under saturation bias conditions, then a short Gaussian ($\sigma = 0.1$ ps) voltage pulse was applied to the gate, and full wave dynamic simulations were performed with $\bar{\tau} = 1$ ps. The resulting dynamic voltage induced at the drain is shown in Figure 8 (right). Note the rapid oscillations that persist in the red curve after the EM energy injected by the Gaussian signal dissipates. Further investigation is required to determine if this behavior indicates plasma oscillations like those observed experimentally in some short channel transistors. It is also worth noting that the oscillations in Figure 8 (right) were not obtainable with the quasi-static approximation. Therefore, if these are indeed THz plasma oscillations, then the full wave EM capabilities of the DVSI/FKT simulation may make it uniquely suited for studying this phenomenon.

To further investigate possible plasma oscillations, the average momentum relaxation lifetime $\bar{\tau}$ can be calculated directly from the semiconductor's electronic band structure and from Fermi's golden rule instead of simply adjusted as an input parameter. In the limit of ballistic transport, the first moment of the BTE

has the form,

$$\frac{\partial \boldsymbol{J}}{\partial t} = \frac{1}{4\pi^3} \int_{\boldsymbol{k}} \boldsymbol{v} \left(q\boldsymbol{E} \frac{df}{dE} - \nabla f \right) \cdot \boldsymbol{v} d\boldsymbol{k}. \tag{19}$$

Comparing this to (18), the transition from ideally diffusive to ballistic transport can be simulated by defining the average momentum relaxation lifetime as,

$$\bar{\tau} = \frac{\int_E \left[\int_{\boldsymbol{k}} \boldsymbol{v}\boldsymbol{v}^T \tau_{\boldsymbol{k}} \rho_{\boldsymbol{k}}(E) d\boldsymbol{k} \right] f dE}{\int_E \left[\int_{\boldsymbol{k}} \boldsymbol{v}\boldsymbol{v}^T \rho_{\boldsymbol{k}}(E) d\boldsymbol{k} \right] f dE}, \tag{20}$$

where the numerator is the flux isosurface integral currently used by the FKT model and the denominator is an additional isosurface integral that can be computed from the band structure's curvature in momentum space. Continued research into plasma oscillations should compute these integrals, along with the other isosurface integrals required by the FKT model, for the InGaAs material system as short gate HEMTs fabricated with these materials have been observed experimentally to exhibit THz emission [45].

In addition to high frequency device physics phenomena, much lower frequency processes important to electronic device applications were also investigated. Efficient, low noise, and linear power amplifiers are required for a broad range of commercial and defense-related applications such as those cited in Section 1. Wide band gap, high breakdown voltage and heat capacity, good thermal conductivity and electron mobility, as well as a high peak electron velocity [65] make GaN well suited for these applications. Furthermore, the spontaneous and piezoelectric polarizations of the GaN/AlGaN material system can produce a highly conductive two-dimensional electron gas in a HEMT structure [66]. For these reasons, the GaN HEMT currently plays a dominant role in RF power amplifier applications [67–71].

Despite its many merits, utilizing the GaN HEMT to its fullest potential requires understanding an operational instability often called the kink effect [72–79]. During a drain voltage sweep, the drain current in the saturation region can appear to be initially suppressed and then increase, over a relatively narrow voltage range, to a higher saturation value. This behavior is concerning, particularly for RF power amplifier design, because the available RF power can be significantly lower than dc characterization might suggest.

To investigate this operational instability, the FKT simulator was further generalized to include field-enhanced direct quantum mechanical tunneling ionization of crystal defects deep in the semiconductor band gap [80–82]. Electron capture and emission by tunneling was expressed as

$$U_{i,\text{tunnel}} = P(|\boldsymbol{E}|) \int \sigma_n v_{th} g(E) N_T \left[f_i(1 - f_T) - (1 - f_i) f_T e^{-E/kT_L} \right] dE, \tag{21}$$

where N_T is trap density, f_T is trap occupation probability, σ_n is the capture cross-section, v_{th} is the mobile electron thermal velocity and $g(E)$ is the density of electron states from the electronic band structure, f_i is the mobile electron distribution function, E_T is the trap energy level, and T_L is the crystal lattice temperature. To approximate the tunneling probability $P(|\boldsymbol{E}|)$ the defect was modeled as a simple square well in a constant electric field, as depicted in Figure 9 (left). The electron wave function Ψ in and around the well was expressed in terms of Airy functions, and $P(|\boldsymbol{E}|) = |\Psi_T/\Psi_C|^2$ approximated the tunneling probability. The wave function inside the trap, i.e. Ψ_T in Figure 9 (left), and the resulting tunneling probability depend on the width of the well approximating the defect. The simplest case is zero width, for which the tunneling probability is,

$$P(|\boldsymbol{E}|) = \text{Ai}\left[-E_T \left(\frac{2m^*}{\hbar^2 q^2 |\boldsymbol{E}|^2} \right)^{1/3} \right] / \text{Ai}[0] \tag{22}$$

where m^* is the semiconductor's effective mass at the conduction band edge. The resulting simulator was applied to a device from the literature designed specifically for studying the kink effect [72]. The simulation computed the drain current I_D versus drain voltage V_D for different gate biases V_G shown in Figure 9 (right) along with measured data from Wang and Chen [72]. The kinks in the simulated drain currents were caused by the direct tunneling ionization of sheet traps under the gate on the AlGaN side of the GaN/AlGaN interface that defines the device's channel. The sudden increase in positively ionized traps has an effect much like an increase in polarization charge at the GaN/AlGaN interface, causing a sudden decrease in threshold voltage and a kink in the drain current. The principal reasons for the tunneling ionization and its voltage dependence are the highly nonlinear field-dependent tunneling probability and ionization's sensitivity to heating of the mobile electrons with which the defect interacts. Therefore, simulating this GaN HEMT behavior requires a charge transport model that can capture the marked electron heating that occurs in these devices in a manner that resolves both subpicosecond hot electron scattering and the widely disparate

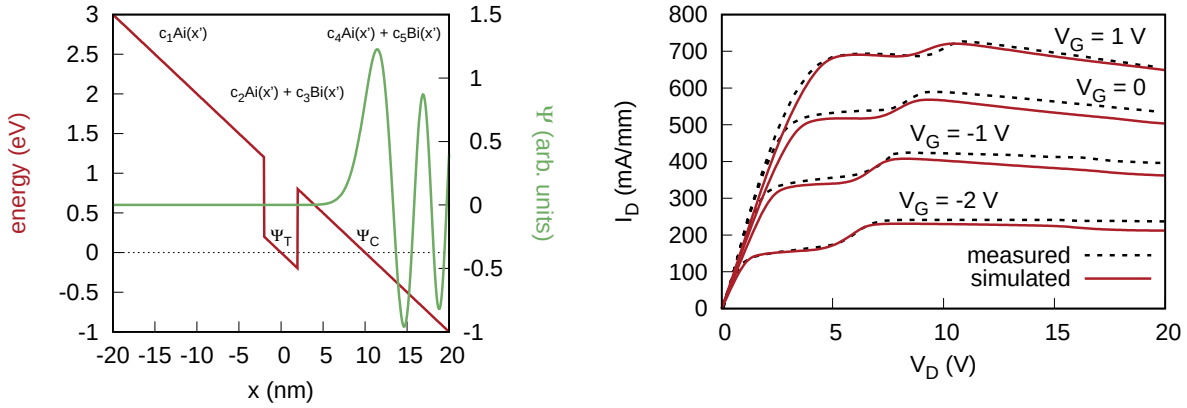

Figure 9: (left) Airy function Schrodinger wave function for an electron trap, approximated as a square potential well, in a constant electric field. The tunneling probability from the conduction band into the trap is approximated as $P(|\boldsymbol{E}|) = |\Psi_T/\Psi_C|^2$. (right) Drain current I_D versus drain voltage V_D for different gate biases V_G. Simulations include field-enhanced ionization of barrier traps under the gate near the GaN/AlGaN interface. The measured data was published by Wang and Chen [72].

deep trap ionization time scales. For these reasons, the FKT simulation appears to be the only computation currently able to capture this important operational instability design concern.

3.3 Circuit-Level Simulation and Characterization

Along with microscopic material properties and macroscopic device simulations, the lab task also made progress in the coupling of devices to their surrounding circuit environments. The results of simulations for large amplitude harmonic input signals can be used to compute various power amplifier circuit metrics such as the maximum power available from the source (23), power delivered to the load (24), power added efficiency (PAE) (25), and transducer gain (26),

$$P_{avs} = \frac{P_{\text{in}}}{1 - \left|\frac{Z_{\text{in}} - Z^*_{\text{source}}}{Z_{\text{in}} + Z_{\text{source}}}\right|^2} \tag{23}$$

$$P_L = \frac{1}{2} V_L I_L^* \tag{24}$$

$$PAE = \frac{P_L - P_{avs}}{I_D^{\text{dc}} V_D^{\text{dc}}} \times 100\% \tag{25}$$

$$G = 10 \log \left(\frac{P_L}{P_{avs}} \right). \tag{26}$$

Because amplifier circuit design considers much larger signal amplitudes than previous S-parameter simulations, some initial tests using a GaN HEMT biased as a class AB amplifier with 50 Ω load resistance investigated possible propagating EM field effects in circuit applications. Results like those in Figure 10 indicate that full wave EM effects can be very significant even at moderate operating frequencies well below the mm-wave range. This is a critical observation because it suggests that effective simulations for designing large signal power amplifier applications must couple full wave EM to hot electron transport, a capability currently available only in the computational tools produced through AFOSR support for this lab task.

Further work on circuit-level design concerns involved experimental characterization to better understand competing performance metrics. Peak performance often requires maximizing one or more competing metrics such as the output power and PAE cited above, as well as the linearity of the circuit over a range of operating conditions. A novel strategy for determining a transistor's bias and impedance which simultaneously optimizes the different metrics was developed. At an initial bias condition, the load and source impedances were tuned to maximize the PAE. Holding these loads constant, the next step determines the optimal bias

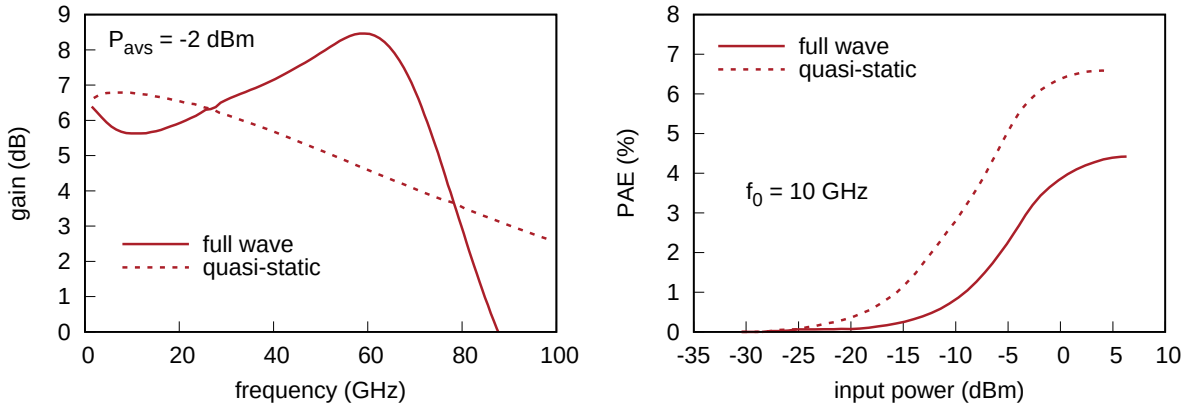

Figure 10: (left) Transducer gain versus frequency for GaN HEMT test structure computed with both full wave and quasi-static electromagnetics. (right) Full wave and quasi-static power added efficiencies for different input powers.

by measuring two-tone power sweeps. The result is a set of power metric contours across the bias space. The optimal bias condition was determined by analyzing the Pareto front [83]. The optimal bias condition is typically the centroid of the Pareto front polygon.

The strategy was applied to an 83 nm gate length GaN HEMT fabricated and tested at AFRL. A maximum 39.9% PAE was measured at the optimal load conditions $\Gamma_S = 0.25\angle 140°$ and $\Gamma_L = 0.72\angle 104°$. All subsequent power measurements were conducted at these tuning points. Input power sweeps were then performed for different quiescent bias conditions. Figure 11 shows the maximum output power, maximum

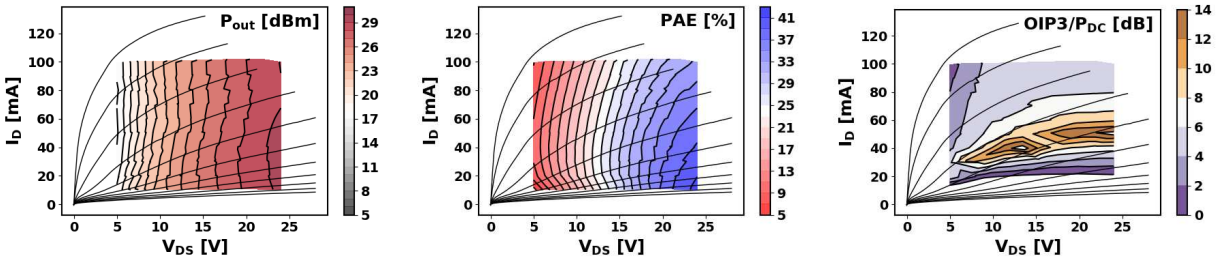

Figure 11: Measured two-tone P_{out} (left), PAE (middle), and OIP3 (right) contours across the I-V plane at 30 GHz fundamental frequency.

PAE, and minimum 3rd order intermodulation (OIP3) as referenced to the dc power. These measured data produce a Pareto optimal bias condition maximizing all three power metrics of $V_{DS} = 25$ V and $I_D = 45$ mA and indicate a useful strategy for identifying conditions for peak MMIC performance. Further research will investigate implementing this strategy through FKT/DVSI device simulation, circumventing the costly device fabrication and experimental characterization.

The investigation of load matching and similar circuit design concerns also extended to devices based on the β-Ga_2O_3 material system [84]. Lateral metal-oxide-semiconductor field-effect transistors (MOSFETs) with 0.5 μm W (tungsten) gates were fabricated on a 65 nm Si-doped β-Ga_2O_3 channel grown by molecular beam epitaxy (MBE) on an Fe-doped substrate. Small and large signal RF power performance was measured to assess its potential for power amplifier applications and to identify limitations to overcome with the aid of physics-based simulation. Operating in the L-band, load pull measurements were made with passive source and load tuning. S-parameters were also measured under pulsed bias conditions. Figure 12 shows output power, transducer gain, and power added efficiency for CW and pulsed measurement conditions. Comparisons of CW and pulsed data suggested the potential for current collapse due to self-heating or drain dispersion, which could act as limitations to performance. Device simulations incorporating the electronic band structure and phonon scattering presented in Section 3.1 may assist in addressing these limitations and

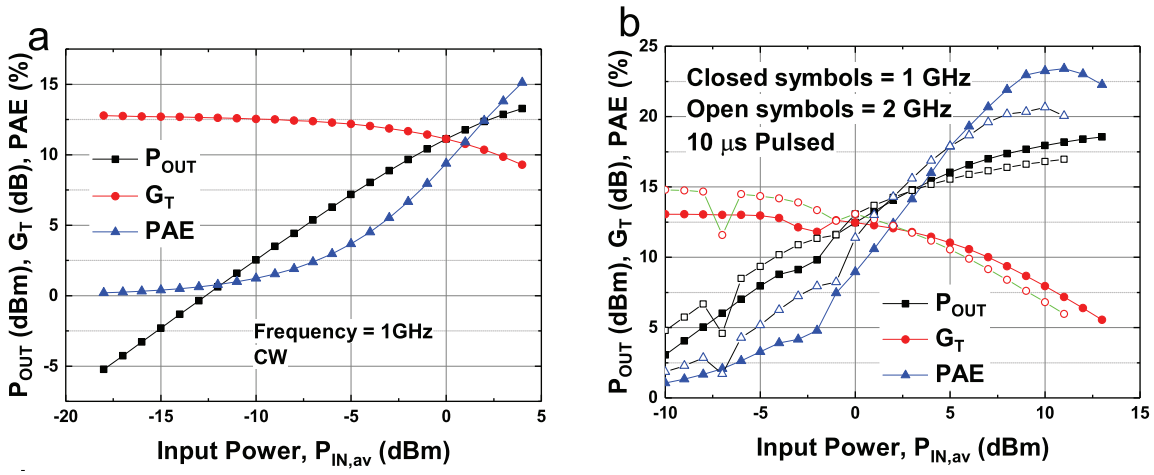

Figure 12: Load-pull power sweeps for CW at 1 GHz (a) and for a 10 μs pulse at 1 GHz and 2 GHz (b).

realizing the potential of this promising device technology.

4 Conclusion

Advanced technologies are essential for supporting the women and men who make the United States Air Force unmatched in capability and effectiveness. In this 21st century digital age, electronics and opto-electronics are indispensable elements of these technologies. Designing them to meet application performance requirements is inevitably a multiscale problem addressing physical concerns ranging from the microscopic atomic scales of material properties to the macroscopic scales of integrated circuits and systems. As such, the design process is often a lengthy and expensive exercise in highly educated trial-and-error. Accurate computational physics tools with predictive capabilities at different levels of the process could possibly reduce the length and cost of the design cycle.

AFOSR support has enabled significant inroads to accurate multiscale computational physics tools. The use of currently existing ab initio tools such as Quantum Espresso has produced accurate electronic band structure and electron-phonon coupling strengths for key electronic materials such as GaN and β-Ga_2O_3. Lab task support has also enabled the development of new computational tools for physics-based device simulation such as a hot electron transport model that can incorporate the microscopic material properties, include the dynamics of crystal defect ionization affecting measured device behavior, and couple to full wave electromagnetic fields necessary for accurate high frequency simulations. These device-level tools have produced simulations of measured device behavior accurate from dc up through the mm-wave frequency range. They have also been able to explain little understood device physics phenomena such as the GaN HEMT kink effect as well as overshoot and drain lag during pulsed gate operation. These capabilities are currently unavailable in other existing academic or commercial device simulation software. Finally, the lab task has made progress with the circuit-level part of the design process. Simulations of devices in different circuit environments has shown the importance of full wave effects for power amplifier design and suggested possible paths towards additional computational tools that may alleviate the dependence on laborious and costly load pull measurements. Continued research on this multiscale design problem and these atoms-to-circuits computational tools may provide a valuable resource for further advancing the Air Force's technological superiority.

References

[1] G. Nikandish, R.B. Staszewski, and A. Zhu, "Breaking the Bandwidth Limit", *IEEE Microw. Mag.*, vol. 21, no. 4, pp. 57–75, April 2020.

[2] R. Gomez-Garcia, "Emerging trends in advanced RF/microwave filters for wireless applications, part I," *IEEE Microw. Mag.*, vol. 21, no. 3, pp. 18–19, March 2020.

[3] N. Zhang, V. Mehrotra, S. Chandrasekaran, B. Moran, L. Shen, U. Mishra, E. Etzkorn, and D. Clarke, "Large area GaN HEMT power devices for power electronic applications: Switching and temperature characteristics," *Power Electronics Specialist Conf.*, vol. 1, pp. 233–237, 2003

[4] Y.F. Wu, B.P. Keller, S. Keller, D. Kapolnek, P. Kozodoy, S.P. Denbaars, and U. Mishra, "High power AlGaN/GaN HEMTs for microwave applications," *Solid-State Electron.*, vol. 41, pp. 1569–1574, 1997.

[5] M.D. Hodge, R. Ventury, J. Shealy, and R. Adams, "A robust AlGaN/GaN HEMT technology for RF switching applications," *Proc. Compound Semicond. Integr. Circ. Symp.*, pp. 1–4, 2011.

[6] P. Saad, R. Hou, R. Hellberg, and B. Berglund, "A 1.8–3.8-GHz power amplifier with 40% efficiency at 8-dB power back-off," *IEEE Trans. Microw. Theory Techn.*, vol. 66, no. 11, pp. 4870–4882, Nov. 2018.

[7] W.P. Pallmann, C.A. Zaugg, M. Mangold, I. Dahhan, M. Golling, B.W. Tilma, B. Witzigmann, and U. Keller, "Ultrafast Electrically Pumped VECSELs," *IEEE Photonics Journal*, vol. 5, no. 4, pp. 1–8, Aug. 2013.

[8] R.G. Bedford, T. Dang, and D. Tomich, "Recent VECSEL Developments for Sensors Applications," *Proc. SPIE*, vol. 8242, San Francisco, CA 2012, pp. 1–8.

[9] P.J. Wellmann, "Power electronic semiconductor materials for automative and energy saving applications–SiC, GaN, Ga_2O_3, and diamond," *Z. Anorg. Allg. Chem.*, vol. 643, pp. 1312-1322, 2017.

[10] M. Califano, "Suppression of Auger Recombination in Nanocrystals via LigandAssisted Wave Function Engineering in Reciprocal Space," *J. Phys. Chem. Lett.*, vol. 9, pp. 2098–2104, 2018.

[11] R. Hui and M. O'Sullivan, **Fiber Optic Measurement Techniques**, Elsevier Academic Press, London, 2009.

[12] P. Roblin, D.E. Root, J. Verspecht, Y. Ko, and J.P. Teyssier, "New trends for the nonlinear measurement and modeling of high-power RF transistors and amplifiers with memory effects," *IEEE Trans. Microw. Theory Techn.*, vol. 60, no. 6, pp. 1964–1978, June 2012.

[13] M. Grupen, "GaN high electron mobility transistor simulations with full wave and hot electron effects," *IEEE Trans. Electron Devices*, vol. 63, no. 8, pp. 3096–3102, Aug. 2016.

[14] M. Cohen and T. Bergstresser, "Band structures and pseudopotential form factors for fourteen semiconductors of the diamond and zincblende structures," *Phys. Rev.*, vol. 141, no. 2, pp. 789–796, 1966.

[15] P. Harrison, **Quantum Wells, Wires, and Dots**, John Wiley & Sons, New York, 2000.

[16] K. Hess, **Advanced Theory of Semiconductor Devices**, IEEE Press, Piscataway, NJ, 2000.

[17] H. Shichijo and K. Hess, "Band-structure-dependent transport and impact ionization in GaAs," *Phys. Rev. B*, vol. 23, no. 8, pp. 4197–4207, 1981.

[18] M. Mohamed, I. Unger, C. Janowitz, R. Manzke, Z. Galazka, R. Uecker, and R. Fornari, "The surface band structure of β-Ga_2O_3," *J. of Phys.: Conf. Series*, vol. 286, pp. 012027, 2011.

[19] H. Peelaers and C.G. Van de Walle, "Brillouin Zone and Band Structure of β-Ga_2O_3," *Phys. Status Solidi B*, vol. 252, no. 4, pp. 828–832, 2015.

[20] N. Marzari and D. Vanderbilt, "Maximally localized generalized Wannier functions for composite energy bands," *Phys. Rev. B*, vol. 56, no. 20, pp. 12847–12865, Nov. 1997.

[21] V.-N. Do, "Non-equilibrium Green function method: theory and application in simulation of nanometer electronic devices," *Adv. Nat. Sci.: Nanosci. Nanotechnol.*, vol. 5, pp. 033001-1–033001-21, June 2014.

[22] F.A. Marino, N. Faralli, T. Palacios, D.K. Ferry, S.M. Goodnick, and M. Saraniti, "Effects of threading dislocations on AlGaN/GaN high-electron mobility transistors," *IEEE Trans. Electron Devices*, vol. 57, no. 1, pp. 353–360, Jan. 2010.

[23] F.N. Donmezer, "Multiscale electro-thermal modeling of AlGaN/GaN heterostructure field effect transistors," Ph.D. Dissertation, Georgia Institute of Technology, 2013.

[24] A. Ashok, D. Vasileska, O.L. Hartin, and S.M. Goodnick, "Electrothermal Monte Carlo simulation of GaN HEMTs including electron-electron interactions," *IEEE Trans. Electron Devices*, vol. 57, no. 3, pp. 562–570, 2010.

[25] J.S. Ayubi-Moak, R. Akis, D.K. Ferry, S.M. Goodnick, and M. Saraniti, "Towards the global modeling of InGaAs-based pseudomorphic HEMTs," *J. Comput. Electron.*, vol. 7, pp. 187–191, Feb. 2008.

[26] J.A. Ferrer Pérez, "Thermal study of GaN-based HEMT," Ph.D. Dissertation, Notre Dame University, 2012.

[27] S. Faramehr, K. Kalna, and Petar Igić, "Drift-diffusion and hydrodynamic modeling of current collapse in GaN HEMTs for RF power application," *Semicond. Sci. Technol.*, vol. 29, pp. 025007–025017, Jan. 2014.

[28] S. Faramehr, K. Kalna, and P. Igić, "Design and simulation of a novel 1400V–4000V enhancement mode buried gate GaN HEMT for power applications," *Semicond. Sci. Technol.*, vol. 29, pp. 115020–115026, Sept. 2014.

[29] S. Strauss, A. Erleback, T. Cilento, D. Marcon, S. Stoffels, and B. Bakeroot, "TCAD methodology for simulation GaN-HEMT power devices," *Proc. 26th Int. Symp. Power Semicond. Devices & ICs*, Waikoloa, Hawaii, June 2014, pp. 257–260.

[30] E.W. Faraclas and A.F.M. Anwar, "AlGaN/GaN HEMTs: Experiment and simulation of dc characteristics," *Solid-State Electron.*, vol. 50, pp. 1051–1056, 2006.

[31] B. Benbakhti, A. Soltani, K. Kalna, M. Rousseau, and J.-C. De Jaeger, "Effects of self-heating on performance degradation in AlGaN/GaN-based devices," *IEEE Trans. Electron Devices*, vol. 56, no. 10, pp. 2178-2185, Oct. 2009.

[32] O. Hartin and Bruce Green, "AlGaN/GaN HEMT TCAD simulation and model extraction for RF applications," *IEEE Biploar/BiCMOS Circ. Tech. Meeting*, Austin, TX, pp. 232–236, Oct. 2010

[33] L. Wang, X. Zhang, G. You, F. Xiong, L. Liang, Y. Hu, A. Chen, J. Liu, and J. Xu, "Modeling the back gate effects of AlGaN/GaN HEMTs," *J. Comput. Electron.*, vol. 13, pp. 872–876, 2014.

[34] S. Stoffels, N. Ronchi, B. De Jaeger, D. Marcon, S. Decoutere, S. Strauss, A. Erlebach, and T. Cilento, "From TCAD device simulation to scalable compact model development for GaN HEMT powerbar designs," *IEEE Workshop on Wide Bandgap Power Dev. and Appl.*, Columbus, OH, pp. 88-91, Oct. 2013.

[35] A. Brannick, N.A. Zakhleniuk, B.K. Ridley, L.F. Eastman, J.R. Shealy, and W.J. Schaff, "Hydrodynamic simulation of surface traps in the AlGaN/GaN HEMT," *Microelec. J.*, vol. 40, pp. 410–412, 2009.

[36] X. Wang, W. Hu, X. Chen, and W. Lu, "The study of self-heating and hot-electrons effects for AlGaN/GaN double-channel HEMTs," *IEEE Trans. Electron Dev.*, vol. 59, no. 5, pp. 1393–1401, 2012.

[37] M. Faqir, G. Verzellesi, G. Meneghesso, E. Zanoni, and F. Fantini, "Investigation of high-electric-field degradation effects in AlGaN/GaN HEMTs," *IEEE Trans. Electron Dev.*, vol. 55, no. 7, pp. 1592–1602, July 2008.

[38] Y. A. Hussein and S. M. El-Ghazaly, "Extending multiresolution time-domain (MRTD) technique to the simulation of high-frequency active devices," *IEEE Trans. Microwave Theory Tech.*, vol. 51, no. 7, pp. 1842–1851, July 2003.

[39] Y. A. Hussein, S. M. El-Ghazaly, and S. M. Goodnick, "An efficient electromagnetic-physics-based numerical technique for modeling and optimization of high-frequency multifinger transistors," *IEEE Trans. Microwave Theory Tech.*, vol. 51, no. 12, pp. 2334–2346, Dec. 2003.

[40] Y. A. Hussein and S. M. El-Ghazaly, "Modeling and optimization of microwave devices and circuits using genetic algorithms," *IEEE Trans. Microwave Theory Tech.*, vol. 52, no. 1, pp. 329–336, Jan. 2004.

[41] M. Movahhedi and A. Abdipour, "Efficient numerical methods for simulation of high-frequency active devices," *IEEE Trans. Microwave Theory Tech.*, vol. 54, no. 6, pp. 2636–2645, June 2006.

[42] M. Grupen, "An alternative treatment of heat flow for charge transport in semiconductor devices," *J. Appl. Phys.*, vol. 106, no. 12, pp. 123702-1–123702-7, Dec. 2009.

[43] M. Grupen, "GaN High Electron Mobility Transistor Simulations With Full Wave and Hot Electron Effects," *IEEE Trans. Electron Dev.*, vol. 63, no. 8, pp. 3096–3102, Aug. 2016.

[44] M. Dyakonov and M. Shur, "Shallow water analogy for a ballistic field effect transistor: New mechanism of plasma wave generation in dc current," *Phys. Rev. Lett.*, vol. 71, no. 15, pp. 2465–2469, Oct. 1993.

[45] W. Knap, J. Lusakowsi, T. Parenty, S. Bollaert, A. Cappy, V.V. Popov, and M.S. Shur, "Terahertz emission by plasma waves in 60 nm gate high electron mobility transistors," *Appl. Phys. Lett.*, vol. 84, no. 13, pp. 2231–2233, March 2004.

[46] Y. Long, Y.-X. Guo, and Z. Zhong, "A 3-D table-based method for non-quasi-static microwave FET devices modeling," *IEEE Trans. on Microw. Theory and Tech.*, vol. 60, no. 10, pp. 3088–3095, 2012.

[47] L. Zhang and M. Chan, "Artificial neural network design for compact modeling of generic transistors," *J. Comput. Electron.*, vol 16, pp. 825–832, April 2017.

[48] I. Angelov, H. Zirath and N. Roshman, "A new empirical nonlinear model for HEMT and MESFET devices," *IEEE Trans. on Microw. Theory and Tech.*, vol. 40, no. 12, pp. 2258–2266, 1992.

[49] D.E. Root, "Future device modeling trends," *IEEE Microw. Mag.*, pp. 45–59, Nov./Dec. 2012;

[50] A. Dasgupta, S. Ghosh, and Y.S. Chauhan, "ASM-HEMT: Compact model for GaN HEMTs," *2015 IEEE Intern. Conf. on Electron Dev. and Solid-State Circ.*, pp. 495–498, 2015.

[51] D.L. Scharfetter and H.K. Gummel, "Large-Signal Analysis of a Silicon Read Diode Oscillator," *IEEE Trans. Electron Dev.*, vol. ED-16, no. 1, pp. 6477, 1969.

[52] S. Sridharan, A. Christensen, A. Venkatachalam, S. Graham, and P.D. Yoder, "Temperature- and doping-dependent anisotropic stationary electron velocity in wurtzite GaN," *IEEE Electron Dev. Lett.*, vol. 32, no. 11, pp. 1522–1525, Nov. 2011.

[53] K. Sarkar and A. Ghosal, "Monte-Carlo study of velocity overshoot and terahertz generation in GaN," *Int. J. Electron. Comm. Tech.*, vol. 2, no. 2, pp. 146–148, June 2011.

[54] F. Dessenne, D. Cichocka, P. Desplanques, and R. Fauquembergue, "Comparison of wurtzite and zinc blende IIIV nitrides field effect transistors: A 2D Monte Carlo device simulation," *Mater. Sci. Eng. B*, vol. 50, no. 1-3, pp. 315–318, Dec. 1997.

[55] B. Geller, A. Hanson, A. Chaudhari, A. Edwards, and I.-C. Kizlyalli, "A broadband low cost GaN-on-silicon MMIC amplifier," in *Proc. IEEE Radio Frequency Integrated Circuits Symp.*, Atlanta, GA, 2008, pp. 123135.

[56] M. Fleischer and H. Meixner, "Gallium Oxide Thin Films: A New Material for High-temperature Oxygen Sensors," *Sens. Actuators B*, vol. 4, pp. 437–441, 1991.

[57] M. Higashiwaki, K. Sasaki, A. Kuramoto, T. Masui, and S. Yamakoshi, "Gallium Oxide Metal Semiconductor Field-effect Transistors on Single-crystal β-Ga_2O_3 (001) Substrate," *Appl. Phys. Lett.*, vol. 100, p. 013504, 2012.

[58] M. Higashiwaki, K. Sasaki, T. Kamimura, M.H. Wong, D. Krishnamurthy, A. Kuramoto, T. Masui, and S. Yamakoshi, "Depletion-mode Ga_2O_3 Metal-oxide-semiconductor Field-effect Transistors on β-Ga_2O_3 Substrates and Temperature Dependence of their Device Characteristics," *Appl. Phys. Lett.*, vol. 103, p. 123511, 2013.

[59] T. Zacherle, P.C. Schmidt, and M. Martin, "Ab Initio Calculations on the Defect Structure of β-Ga_2O_3," *Phys. Rev. B*, vol. 87, p. 235206, 2013.

[60] A.S. Christensen, T. Kuba, Q. Cui, and M. Elstner, "Semiempirical Quantum Mechanical Methods for Noncovalent Interactions for Chemical and Biochemical Applications," *Chem. Rev.*, vol. 116, pp. 5301–5337, 2016.

[61] J.C. Slater and G.F. Koster, "Simplified LCAO method for the periodic potential problem," *Phys. Rev.*, vol. 94, pp. 1498–1524, 1954.

[62] J.B. Varley, J.R. Weber, A. Janotti, and C.G. Van de Walle, "Oxygen vacancies and donor impurities in β-Ga_2O_3," *Appl. Phys. Lett.*, vol. 97, p. 142106, 2010.

[63] M.D. Santia, D.C. Look, and S.C. Badescu, "Electron-phonon coupling and electron mobility in degenerately doped oxides from first-principles," *Optical Engineering*, vol. 59, no. 6, pp. 067103-1–067103-13, June 2020.

[64] S. Ponce, E.R. Margine, C. Verdi, F. Giustino, "EPW: electron-phonon coupling, transport and superconducting properties using maximally localized Wannier functions," *Comput. Phys. Commun.*, vol. 209, pp. 116–133, Aug. 2016.

[65] D.J. Meyer, D.A. Deen, D.F. Storm, M.G. Ancona, D.S. Katzer, R. Bass, J.A. Roussos, B.P. Downey, S.C. Binari, T. Gougousi, T. Paskova, E.A. Preble, and K.R. Evans, "High electron velocity submicrometer AlN/GaN MOS-HEMTs on freestanding GaN substrates," *IEEE Electron Device Lett.*, vol. 34, no. 2, pp. 199–201, Feb. 2013.

[66] O. Ambacher, J. Smart, J.R. Shealy, N.G. Weimann, K. Chu, M. Murphy, W.J. Schaff, L.F. Eastman, R. Dimitrov, L. Wittmer, M. Stutzmann, W. Rieger, and J. Hilsenbeck, "Two-dimensional electron gases induced by spontaneous and piezoelectric polarization charges in N- and Ga-face AlGaN/GaN heterostructures," *J. Appl. Phys.*, vol. 85, no. 6, pp. 3222–3233, March 1999.

[67] M. Kuzuhara and M. Tokuda, "Low-loss and high-voltage III-nitride transistors for power switching applications," *IEEE Trans. Electron Devices*, vol. 62, no. 2, pp. 405–413, Feb. 2015.

[68] T.J. Flack, B.N. Pushpakaran, and S.B. Bayne, "GaN technology for power electronic applications: A review," *J. Electron. Mater.*, vol. 45, no. 6, pp. 2673–2682, Jun. 2016.

[69] U.K. Mishra, L. Shen, T.E. Kazior, and Y.-F. Wu, "GaN-based RF power devices and amplifiers," *Proc. IEEE*, vol. 96, no. 2, pp. 287–305, Feb. 2008.

[70] U.K. Mishra, P. Parikh, and Y.-F. Wu, "AlGaN/GaN HEMTs: An overview of device operation and applications," *Proc. IEEE*, vol. 90, no. 6, pp. 1022–1031, June 2002.

[71] R.S. Pengelly, S.M. Wood, J.W. Milligan, S.T. Sheppard, and W.L. Pribble, "A review of GaN on SiC high electron-mobility power transistors and MMICs," *IEEE Trans. Microwave Theory and Tech.*, vol. 60, no. 6, pp. 1764–1783, June 2012.

[72] M. Wang and K.J. Chen, "Kink Effect in AlGaN/GaN HEMTs Induced by Drain and Gate Pumping," *IEEE Electron Device Lett.*, vol. 32, no. 4, pp. 482–484, April 2011.

[73] J.K. Kaushik, V.R. Balakrishnan, B.S. Panwar, and R. Muralidharan, "On the origin of kink effect in current-voltage characteristics of AlGaN/GaN high electron mobility transistors," *IEEE Trans. Electron Devices*, vol. 60, no. 10, pp. 3351–3357, Oct. 2013.

[74] G. Meneghesso, F. Zanon, M.J. Uren, and E. Zanoni, "Anomalous kink effect in GaN high electron mobility transistors," *IEEE Electron Dev. Lett.*, vol. 30, no. 2, pp. 100–102, Feb. 2009.

[75] M. Xiao-Hua, L. Min, P. Lei, J. Yuan-Qi, Y. Jing-Zhi, C. Wei-Wei, and L. Xin-Yu, "Kink effect in current-voltage characteristics of a GaN-based high electron mobility transistor with an AlGaN back barrier," *Chin. Phys. B*, vol. 23, no. 2, pp. 027302-1–027302-4, 2014.

[76] M. Singh, M.J. Uren, T. Martin, S. Karboyan, H. Chandrasekar, and M. Kuball, "'Kink' in AlGaN/GaN-HEMTs: Floating buffer model," *IEEE Trans. Electron Devices*, vol. 65, no. 9, Sep. 2018.

[77] H. Hirshy, M. Singh, M.A. Casbon, R.M. Perks, M.J. Uren, T. Martin, M. Kuball, and P.J. Tasker, "Evaluation of pulsed IV analysis as validation tool of nonlinear RF models of GaN-based HFETs," *IEEE Trans. Electron Devices*, vol. 65, no. 12, pp. 5307–5313, Dec. 2018.

[78] P. Altuntas, N. Defrance, M. Lesecq, A. Agboton, R. Ouhachi, E. Okada, C. Gaquiere, J.-C. De Jaeger, E. Frayssinet, and Y. Cordier, "On the correlation between kink effect and effective mobility in InAlN/GaN HEMTs," *Proc. 9th European Microw. Integrated Circuits Conf.*, Rome, Italy, Oct. 2014, pp. 88–92.

[79] C. Sharma, R. Laishram, Amit, D.S. Rawal, S. Vinayak, and R. Singh, "Investigation on de-trapping mechanisms related to non-monotonic kink pattern in GaN HEMT devices," *AIP Advances*, vol. 7, pp. 085209-1–085209-5, Aug. 2017.

[80] S.D. Ganichev, I.N. Yassievich, W. Prettl, J. Diener, B.K. Meyer, and K.W. Benz, "Tunneling Ionization of Autolocalized DX^- Centers in Terahertz Fields," *Phys. Rev. Lett.*, vol. 75, no. 8, pp. 1590–1593, Aug. 1995.

[81] S.D. Ganichev, E. Ziemann, W. Prettl, I.N. Yassievich, A.A. Istratov, and E.R. Weber, "Distinction between the Poole-Frenkel and tunneling models of electric-field-stimulated carrier emission from deep levels in semiconductors," *Phys. Rev. B*, vol. 61, no. 15, pp. 10361–10365, April 2000.

[82] M. Grupen, "Reproducing GaN HEMT Kink Effect by Simulating Field Enhanced Barrier Defect Ionization," *IEEE Transactions on Electron Devices*, vol. 66, no. 9, pp. 3777–3783, Sept. 2019.

[83] J. Martin, C. Baylis, L. Cohen, J. de Graaf, and R.J. Marks II, "A Peak-search Algorithm for Load-pull Optimization of Power-added Efficiency and Adjacent-channel Power Ratio," *IEEE Trans. Microwave Theory and Tech.*, vol. 62, no. 8, pp. 1772–1783, Aug. 2014.

[84] N.A. Moser, T. Asel, K.J. Liddy, M. Lindquist, N.C. Miller, S. Mou, A. Neal, D.E. Walker, S. Tetlak, K.D. Leedy, G.H. Jessen, A.J. Green, and K.D. Chabak, "Pulsed Power Performance of β-Ga_2O_3 MOSFETs at L-Band," *IEEE Electron Dev. Lett.*, vol. 41, no. 7, pp. 989–992, July 2020.

Appendix A: In-House Activities

Personnel:

Name	Emp. Type	Field	Role	Involvement
Dr. M. Grupen	Civ.	Electrical Engineering	Theory & Sim.	60%
Dr. N. Miller	Civ.	Electrical Engineering	Theory & Sim	40%
Dr. S. Badescu	Civ.	Physics	Theory & Sim	35%
Dr. N. Usechak	Civ.	Optical Engineering	Theory & Sim	5%

Publications:

1. A.J. Green, N. Moser, **N.C. Miller**, K.J. Liddy, M. Lindquist, M. Elliot, J.K. Gillespie, R.C. Fitch, Jr., R. Gilbert, D.E. Walker, Jr., E. Werner, A. Crespo, E. Beam, A. Xie, C. Lee, Y. Cao, and K.D. Chabak, "RF Power Performance of Sc(Al,Ga)N/GaN HEMTs at Ka-Band," *IEEE Electron Dev. Lett.*, vol. 41, no. 8, pp. 1181–1184, Aug. 2020.

2. N.A. Moser, T. Asel, K.J. Liddy, M. Lindquist, **N.C. Miller**, S. Mou, A. Neal, D.E. Walker, S. Tetlak, K.D. Leedy, G.H. Jessen, A.J. Green, and K.D. Chabak, "Pulsed Power Performance of β-Ga_2O_3 MOSFETs at L-Band," *IEEE Electron Dev. Lett.*, vol. 41, no. 7, pp. 989–992, July 2020.

3. D.C. Look, K.D. Leedy, R.-H. Horng, M.D. Santia, and **S.C. Badescu**, "Electrical and optical properties of degenerate and semi-insulating ZnGa2O4: Electron/phonon scattering elucidated by quantum magnetoconductivity," Editor's Pick *Appl. Phys. Lett.*, vol. 116, pp. 252104-1–252104-5, June 2020.

4. J. Anders, M. Kaximierczuk, K. Leedy, N. Miller, T. Cooper, M. Streby, and M. Schuette, "Gated Hall and field-effect transport characterization of e-mode ZnO TFTs," *Appl. Phys. Lett.*, vol. 116, pp. 252105-1–252105-4, June 2020.

5. M.D. Santia, D.C. Look, and **S.C. Badescu**, "Electron-phonon coupling and electron mobility in degenerately doped oxides from first-principles," *Opt. Eng.*, vol. 59, no. 6, pp. 067103-1–067103-13, June 2020.

6. N.A. Blumenschein, N.A. Moser, E.R. Heller, **N.C. Miller**, A.J. Green, A. Popp, A. Crespo, K. Leedy, M. Lindquist, T. Moule, S. Dalcanale, E. Mercado, M. Singh, J.W. Pomeroy, M. Kuball, G. Wagner, T. Paskova, J.F. Muth, K.D. Chabak, and G.H. Jessen, "Self-heating characterization of β-Ga_2O_3 thin-channel MOSFETs by pulsed I-V and Raman nanothermography," *IEEE Trans. Electron Dev.*, vol. 67, no. 1, pp. 204–211, Jan. 2020.

7. K.D. Chabak, K.D. Leedy, A.J. Green, S. Mou, A.T. Neal, T. Asel, E.R. Heller, N.S. Hendricks, K. Liddy, A. Crespo, **N.C. Miller**, M.T. Lindquist, N.A. Moser, R.C. Fitch Jr., D.E. Walker Jr., D.L. Dorsey, and G.H. Jessen, "Lateral β-Ga_2O_3 field effect transistors," *Semicond. Sci. Tech.*, vol. 35, pp. 013002-1–013002-22, Nov. 2019.

8. D.C. Look, K.D. Leedy, M.D. Santia, and **S.C. Badescu**, "Characterization of layer/substrate interface quality via quantum-based magnetoconductivity: application to ITO on fused silica," submitted to *Nature Materials*.

9. S.G. Carter, **S.C. Badescu**, A.S. Bracker, M.K. Yakes, K.X. Tran, J.Q. Grim, and D. Gammon, "Coherent optical control of quantum dot hole spins using triplet trion states," submitted to *Phys. Rev. Lett.*

10. K. Mahalingam , K.G. Eyink, B. Athey, B. Urwin, S. Pacley, and **S.C. Badescu**, "Spontaneous Atomic Ordering in $(Al_xGa_{1-x})_2O_3$ Films Grown on (010) β-Ga_2O_3 Substrates," submitted to *Appl. Phys. Lett.*

11. **M. Grupen**, "Reproducing GaN HEMT Kink Effect by Simulating Field Enhanced Barrier Defect Ionization," *IEEE Transactions on Electron Devices*, vol. 66, no. 9, pp. 3777–3783, Sept. 2019.

12. D. Hashemi, G. Siegel, M. Snure, **S.C. Badescu**, "Vicinal Metal Surfaces as Potential Catalysts for Phosphorene Epitaxial Growth," *Applied Physics Letters*, vol. 115, no. 11, pp. 113104-1–113104-5, Sept. 2019.

13. M. Snure, T. Prusnick, E. Bianco, **S.C. Badescu**, "A Computational and Experimental Investigation of the Phonon and Optical Properties of Au_2P_3," *Materials*, vol. 12, no. 4, pp. 555–562, Feb. 2019.

14. J. Lee, S. Ganguli, A.K. Roy, and **S.C. Badescu**, "Density Functional Tight Binding Study of βGa_2O_3: Electronic Structure, Surface Energy, and Native Point Defects," *Journal of Chemical Physics*, vol. 150, no. 17, pp. 174706-1–174706-8, May 2019.

15. **N.C. Miller**, **M. Grupen**, K. Beckwith, D. Smithe, and J.D. Albrecht, "Computational Study of Fermi Kinetics Transport Applied to Large-signal RF Device Simulations," *Journal of Computational Electronics*, vol. 17, no. 4, pp. 1658–1675, Dec. 2018.

16. J. Hader, **S.C. Badescu**, L.C. Barrow, J.V. Moloney, S.R. Johnson, and S.W. Koch, "Auger Losses in Dilute InAsBi," *Appl. Phys. Lett.*, vol. 112, p. 192106, 2018.

17. J. Hader, **S.C. Badescu**, L.C. Bannow, J.V. Moloney, S.R. Johnson, and S.W. Koch, "Extended Band Anti-crossing Model for Dilute Bismides," *Appl. Phys. Lett.*, vol. 112, p. 062103, 2018.

18. L.C. Bannow, **S.C. Badescu**, J. Hader, J.V. Moloney, and S.W. Koch, "Light-hole - Heavy-hole Splitting in Bulk Dilute Bismides,", *Appl. Phys. Lett.*, vol. 111, p. 182103, Oct. 2017.

19. L.C. Bannow, **S.C. Badescu**, J. Hader, J.V. Moloney, and S.W. Koch, "Valence Band Splitting in Bulk Dilute Bismides," *Appl. Phys. Lett.*, vol. 111, p. 182103, 2017.

20. G. Siegel, C.V. Ciobanu, B. Narayanan, M. Snure, and **S.C. Badescu**, "Heterogeneous pyrolysis: a route for epitaxial growth of hBN atomic layers on copper using separate boron and nitrogen precursors," *Nano Letters*, vol. 17, no. 4, p. 2404, 2017.

21. Y. Oshima, E. Ahmadi, **S.C. Badescu**, F. Wu, and J.S. Speck, "Composition determination of $\beta(Al_xGa_{1-x})_2O_3$ layers coherently grown on (010) β-Ga_2O_3 substrates by high-resolution X-ray diffraction," *Applied Physics Express* vol. 9, p. 061102, 2016.

22. L.C. Bannow, O. Rubel, **S.C. Badescu**, P. Rosenow, J. Hader, J.V. Moloney, R. Tonner, and S.W. Koch, "Configuration dependence of band-gap narrowing and localization in dilute GaAs 1x Bi x alloys," *Phys. Rev. B*, vol. 93, p. 205202, 2016

23. J. Hader, J.V. Moloney, O. Rubel, **S.C. Badescu**, S. Johnson, and S.W. Koch, "Microscopic modelling of opto-electronic properties of dilute bismide materials for the mid-IR," *Proc. SPIE 9767, Novel in-Plane Semiconductor Lasers XV*, p. 976709, 2016.

Presentations:

1. D.C. Look, K.D. Leedy, R.-H. Horng, M.D. Santia, and **S.C. Badescu**, "Electron mobility from phonon scattering in degenerate semiconductors: ZnO, β-Ga_2O_3, and $ZnGa_2O_4$," invited talk Proceedings of Oxide-based Materials and Devices XI, 2020.

2. **S.C. Badescu**, M.D. Santia, D.C. Look, and K.D. Leedy, "First-principles modeling of native point defects in zinc gallate," invited talk Proceedings of Oxide-based Materials and Devices XI, 2020.

3. M.D. Santia, D.C. Look, and **S.C. Badescu**, "Electron-phonon coupling and electron mobility in degenerately doped oxides from first-principles," invited talk Proceedings of Oxide-based Materials and Devices XI, 2020.

4. **C.S. Badescu**, invited talk "Modeling of phase transitions in aluminum-gallium oxide alloys," Proceedings of SPIE, vol. 10919 Oxide-based Materials and Devices X, San Francisco, CA, March 2019.

5. **M. Grupen**, **N.C. Miller**, and J. Albrecht, "Investigating the 'Kink Effect' in GaN HEMT Technology Using Fermi Kinetics Transport," *20th International Workshop on Computational Nanotechnology*, Evanson, Illinois, May 2019.

6. **N.C. Miller**, N. Moser, G.D. Via, R. Fitch, J. Gillespie, A. Green, D. Walker, Jr., A. Crespo, M. Schuette, and K. Chabak, "Optimizing the Bias and Impedance Trade Space for High Power and High Linearity GaN HEMTs," accepted by GOMACTech 2020, San Diego, CA, March 2020.

7. **S.C. Badescu** and **M. Grupen**, "Electronic Bandstructures at the Interface Between ϵ-$(Me_xGa_{1-x})_2O_3$ (Me = Al, In) and Insulating Substrates," *60th Electronic Materials Conference*, University of California, Santa Barbara, June 2018.

8. D. Hashemi, J. Lee, **S.C. Badescu**, and **M. Grupen**, "Electronic Bandstructures at the Interface Between ϵ-$(Me_xGa_{1-x})_2O_3$ (Me = Al, In) and Insulating Substrates," *3rd US Workshop on Gallium Oxide*, The Ohio State University, Columbus, OH, Aug. 2018.

9. **N. Miller**, **M. Grupen**, and S. Wong "Advanced Semiconductor Device Modeling on the HPC," at the *2018 DoD High Performance Computing (HPC) User Group Meeting*, Air Force Institute of Technology, Wright-Patterson AFB, Sept. 2018.

10. **M. Grupen**, "Physics-Based Methods for High Frequency GaN HEMT Simulation," invited talk at *Advances in GaN Device Technology for Millimeter-wave Applications Workshop, European Microwave Week*, Nuremberg, Germany, Oct. 2017.

11. **S.C. Badescu**, "First principles bandstructures of ternary and quaternary bismide-containing semiconductors," invited talk at *8th International Workshop on Bismuth-Containing Semiconductors*, Marburg University, Germany, July 23–26 2017.

12. **N.C. Miller**, J.D. Albrecht, D. Smithe, K. Beckwith, and **M. Grupen**, "A Numerical Study of Fermi Kinetics Transport," *International Workshop on Computational Nanotechnology*, Windermere, UK, June 2017.

13. **S.C. Badescu**, "First Principles Modeling of Emerging Materials for Electronics Applications," invited talk at AFOSR workshop on *Enhancing International Collaborations on Emerging Materials for defense Applications via Innovative Theory, Simulation, and Experiment*, University College London, UK, July 2016.

Awards and Professional Activities:

72nd Annual Arthur S. Flemming Award (Usechak)

IEEE Dayton Section Harrel V. Nobel Award for physics-based modeling (Miller)

Scientific Advisory Board Best Presentation Award, "Physics-based Device Modeling" (Miller)

2018 IEEE Photonics Society Award (Usechak)

STTR topic "High Speed Electronic Device Simulator" (Grupen)

Team Lead for DARPA DREaM verification and validation measurement group (Miller)

Manager of in-house GaN140 PDK (Miller)

Managing in-house ASM-HEMT model development with contractor Keysight Technologies (Miller)

Program Officer for "High Speed Electronic Device Simulator" STTR Phase 2 awarded to TechX/Michigan State University (Grupen, Miller)

NRC Research Advisor (Grupen, Badescu, Usechak)

IEEE Electron Device Letters reviewer (Grupen, Miller)

Managed KPP measurements and evaluations of GaN transfer Mantech effort (Miller)

DoD HPCMP project manager (Miller)

Managing Keysight ADS PDK for the in-house GaN process (Miller)

Technical Advisor for SOCHE student Bendic Pacia (Miller, Grupen)

Advisor for on-site Post-doctoral Fellow Dr. Daniel Hashemi (Badescu)

Advisor for on-site Post-doctoral Fellow Dr. Marco Santia (Badescu)

IEEE AVFOP GOMAC Session Chair, Albuquerque, NM (Usechak)

Optics Letters reviewer (Usechak)

Optics Express reviewer (Usechak)

Journal of Selected Topics in Quantum Electronics reviewer (Usechak)

Government Program Manager and CTO for $112.5M AIM Photonics Program (Usechak)

Reviewer, SME, and Contract Officer Representative for DARPA/STO (Usechak)

Reviewer, SME, and Contract Officer Representative for DARPA/MTO (Usechak)

Author and Program Manager for $2.25M SBIR Phase II topic "Scalable Coherent Photonic Array on a Silicon Platform" (Usechak)

Author and Program Manager for $10.55M SBIR Phase III topic "Coherent Homodyne Integrated RF-photonic Systems (CHIPS)" (Usechak)

Author and Program Manager for $10.55M SBIR Phase III topic "40 GHz Instantaneious Wideband Spectrum Monitoring System" (Usechak)

Author and Program Manager for AFRL's $6M RIPTIDE Program spread over four different contracts (Usechak)

Scientific Advisory Board Briefing, "RF Photonics and Integrated Photonic Circuits" (Usechak)

IEEE Microwave Theory and Techniques reviewer (Miller)

IEEE Transactions on Electron Devices reviewer (Grupen)

Reviewer for AFOSR computer simulation proposals (Grupen)

Reviewer for DARPA Texitronics program (Badescu, Grupen)

Mentor for UC Merced summer intern Andrew Jacobs (Badescu)

IEEE AVFOP GOMAC Session Chair, Miami, FL (Usechak)

Advisor for Visiting Summer Faculty Fellow Prof. Cristian V. Ciobanu Colorado School of Mines (Badescu)

Advisor for summer student intern Jacob Tavenner Colorado School of Mines (Badescu)

Advisor for SMART student program (Grupen)